An Electrode Design Rule for Organic Photovoltaics Elucidated Using a Low Surface Area Electrode

*G. Dinesha M. R. Dabera, Jaemin Lee, Ross A. Hatton**

Dr. G. Dinesha M. R. Dabera, Dr. Jaemin Lee, Dr. Ross A. Hatton

Department of Chemistry, University of Warwick, Gibbet Hill Road, Coventry CV4 7AL, United Kingdom

E-mail: ross.hatton@warwick.ac.uk

Dr. G. Dinesha M. R. Dabera

Present address: Warwick Manufacturing Group (WMG), University of Warwick, Gibbet Hill Road, Coventry CV4 7AL, United Kingdom

Keywords: transparent electrode, nanoparticle electrode, organic photovoltaic, organic solar cell, gold nanoparticle, polymer solar cell

It is widely considered that charge carrier extraction in bulk-heterojunction organic photovoltaics (BHJ OPVs) is most efficient when the area of contact between the semiconductor layers and the electrodes is maximized and the electrodes are electrically homogeneous. Herein, we show that ~ 99% of the electrode surface can in fact be insulating without degrading the efficiency of charge carrier extraction, provided the spacing of the conducting areas is less than or equal to twice the optimal thickness of the BHJ layer. This striking result is demonstrated for BHJ OPVs with both conventional and inverted device architectures using two different types of BHJ OPVs: namely PCDTBT:$PC_{70}BM$ and the ternary blend PBDB-T:ITIC-m:$PC_{70}BM$. This finding opens the door to the use of a large pallet of materials for optical spacers and charge transport layers, based on a low density of conducting particles embedded in a wide band gap insulating matrix.

1. Introduction

Solution processed OPVs that use an interpenetrating blend of electron-donor and electron acceptor type organic semiconductors (i.e. a bulk-heterojunction) as the light harvesting layer have achieved a certified power conversion efficiency of 15.8%[1] and 17.3%[2] in single-junction and multi-junction architectures respectively, with the latter being sufficient for commercial applications. The efficiency of charge carrier extraction by the electrodes in these devices is a key determinant of device power conversion efficiency (PCE) and is known to depend in a complex way on a number of electrode properties including work function, surface micro-structure, surface energy and surface roughness [3]. However, systematic variation of one of these parameters whilst controlling all others is inherently challenging in device based experiments and so many aspects of the science of electrode-organic semiconductor interfaces still remain the subject of debate [4].

In bulk-heterojunction (BHJ) OPVs conventional wisdom dictates that the electrode should be smooth, so not to risk undermining the integrity of the diode, and the whole surface should have a uniformly high electrical conductivity [5]. Indium-tin oxide (ITO) coated glass meets these requirements, which, together with its high transparency, is why it is the substrate electrode of choice for research into OPVs. However, it is widely considered that for most practical applications of OPVs ITO glass is prohibitively expensive and so there is considerable interest in the development of alternatives including electrodes based on carbon nanotubes [3a] and metal nanowire networks [6] which are inherently heterogeneous in their conductivity across their surface and so are invariably used in conjunction with a highly conducting over layer. To our knowledge it is not known as to what extent the surface area of the substrate electrode in OPVs can be reduced by making a portion of the surface electrically insulating without eroding the efficiency of charge carrier extraction, or whether a reduction in the area in contact with the semiconductors layer may in fact be beneficial. Herein, we report the findings of a study which

sheds light on this fundamental question, and discuss the implications for the design of optical spacers and large nanoparticle and nanowire based electrodes for OPVs.

For the purpose of this study we have designed a model transparent electrode as a research tool, the structure of which is shown in **Figure 1** together with the process for electrode fabrication. The electrode comprises a low sheet resistance (15±3 Ohms per square), low surface roughness (root-mean-square roughness ~0.7 nm) ITO glass substrate covered with a layer of the insulating transparent polymer polymethylmethacrylate (PMMA) that is thick enough to electrically isolate the underlying ITO electrode from the semiconductor layers in the device. Embedded within the PMMA layer are gold nanoparticles (AuNPs) which are in contact with the underlying ITO and also protrude from the polymer surface. Consequently electrons can only cross the AuNP/PMMA layer at the site of AuNPs, and the surface area of the electrode in contact with the semiconductor layers is determined by the AuNP density.

2. Results and Discussion

2.1 Small area electrode design & fabrication

In order to guarantee that all AuNPs were electrically connected to the ITO substrate they were chemically tethered to the surface using the small molecule 3-mercaptopropyltrimethoxysilane (MPTMS) [7], followed by deposition of the PMMA layer by spin coating over the whole surface. The PMMA layer was then etched uniformly by UV/O_3 treatment to a thickness of ~10 nm, exposing the top of the tethered AuNPs, a process that inevitably also results in removal of the citrate ligand at the surface of the AuNPs. Finally the PMMA surface (with protruding AuNPs) was conformably covered with 5 nm thick MoO_{3-x} deposited by thermal evaporation. This very thin MoO_{3-x} layer ensures optimised interfacial energetics for hole-extraction [8] but is too resistive to enable significant lateral charge transport due to its very low conductivity and very low thickness: The conductivity of vacuum evaporated MoO_{3-x} is < 10^{-7} S cm^{-1}, which limits its useful thickness in OPVs to < 20 nm [9]. For the thickness used in this context (5 nm) the sheet

resistance would therefore be $\geq 10^{13}$ Ohm sq^{-1}. The very thin MoO_{3-x} layer does however serve to ensure that the PMMA is not dissolved during deposition of the organic semiconductor layers. The conducting atomic force microscopy (c-AFM) image in Fig. 2b shows that the electrode surface is very insulating except at the site of the AuNPs. Due to the size distribution of the AuNPs particles (Figure S1) some of the AuNPs protrude several nanometres from the PMMA surface, as can be seen from the AFM height image (**Figure 2a**). For the purpose of this study the mean diameter of AuNPs was chosen to be 14 nm ± 4 nm because this size is too small to significantly scatter light[10], whilst being large enough to protrude through the 10 nm PMMA layer. Also, because the AuNPs are embedded in the transparent PMMA layer they are not expected to contribute significantly to near field plasmonic enhancement in photocurrent, since the light is most strongly concentrated on the sides of the AuNPs embedded in PMMA layer [11].

2.2 OPV device studies

In the first instance this model electrode was incorporated into OPV devices based on the well characterized bulk-heterojunction PCDTBT:$PC_{70}BM$ [12]. Devices were fabricated with the architecture; ITO/MoO_{3-x} (5 nm)/PCDTBT:$PC_{70}BM$(80 nm)/BCP(4.5 nm)/Al(100 nm) with and without AuNPs/PMMA (10 nm) at the ITO/MoO_{3-x} interface. The thicknesses of each of the organic semiconductor layers used is that reported to give optimal device performance [13]. Representative AFM images showing the distribution of AuNPs as a function of nanoparticle concentration used in devices are given in Figure S2. The performance characteristics with respect to the percentage conducting area and average inter-particle distance (See Supporting Information for calculation of these parameters) are shown in **Figure 3**. The data in Figure 3 (and Table S1, Figure S3) for reference devices corresponds to that collected immediately after illuminated with AM 1.5G simulated solar irradiation, because device performance deteriorates with time under constant illumination (Table S2), which is typical of PCDTBT:$PC_{70}BM$ based

OPVs[14]. Tournebize *et al*,[14b] attribute this photo-degradation to the formation of polycarbazolyl radicals within the PCDTBT domains and their subsequent trapping by $PC_{70}BM$, whilst Peters *et al*[14a] have shown that it stems from photo-induced formation of sub - bandgap states within the active layer. Given that both of these degradation mechanisms are associated with the bulk-heterojunction it is reasonable to expect that they also occur in devices incorporating an AuNP/PMMA layer. However, OPV devices with an AuNP/PMMA layer actually substantially improve with increasing illumination up to a time of 50 minutes, due to an increase in fill-factor (FF) and short circuit current density (J_{sc}): Figure S4, Figure S5. Consequently, the data in Figure 3 for devices incorporating an AuNP/PMMA layer correspond to that recorded after 50 min constant illumination. The improvement in FF is due to a reduction in device series resistance (Figure S4) which accounts for the ~1 mA cm^{-2} improvement in J_{sc}. To confirm that the increase in J_{sc} does not result from breakdown of the insulating PMMA layer, OPV devices with the structure: ITO/PMMA (10 nm)/MoO_{3-x}(5 nm)/PCDTBT:$PC_{70}BM$ (80 nm)/BCP (4.5 nm)/Al (100 nm) were fabricated and measured over 1 hour under constant illumination. Over this period of time no significant photo-current was measured (Figure S6) and so the improvement in J_{sc} cannot be due to electrical breakdown of the PMMA layer. The reduction in series resistance of devices incorporating AuNPs upon illumination is likely due to reduced contact resistance between the AuNPs and the underlying ITO glass, possibly due to electromigration of Au atoms over the AuNP surface [15], a process that would be accelerated by the inevitable heating of the AuNPs that occurs due to relaxation of the localised surface plasmon resonance excitation [16]. Alternatively, it may result from reduction of the thin gold oxide layer that forms at the surface of the AuNPs upon UV/O_3 treatment, which can persist for an extended period before reducing back to Au^0[11b]. Regardless of which mechanism is responsible for the reduction in series resistance during the first 50 minutes of illumination, the variation in device performance with AuNP density in Figure 3 shows that for efficient hole-extraction it is not necessary for the entire electrode surface to be electrically conducting. When

the average separation between conducting regions is ~240 nm (equivalent to an electrode area of only ~0.2%) the average device performance saturates at a value comparable to that of devices using an ITO electrode without an AuNP/PMMA interlayer: 4.24% ± 0.42% (with AuNP/PMMA) *vs* 4.04% ±0.19 % (without AuNP/PMMA). Indeed, champion devices using an AuNP/PMMA electrode substantially outperform those without: PCE of 4.74% and 4.15% respectively (Table S1). Notably, it is evident from Figure 3 that the critical inter-particle separation to achieve a performance comparable to that of the reference is approximately twice that of the maximum thickness for an active layer of PCDTBT:$PC_{70}BM$ (~110 nm)[13b]. Since it is likely that the mechanisms that gives rise to continuous degradation in performance of reference devices are also operative in devices with an AuNP/PMMA interlayer, the optimal performance of the latter may in fact be substantially higher if 50 minutes of constant illumination was not required.

It is evident from **Figure 4(a)** and Figure S7 that there is no significant difference in the shape of the external quantum efficiency (EQE) spectra for devices with and without the AuNP/PMMA interlayer, which is consistent with the expectation that the photocurrent is not inflated by plasmon enhanced light absorption due to the presence of AuNPs. Additionally, transfer matrix modelling of the optical intensity in the device with and without a 10 nm layer of PMMA (Figure 4(b) and (c)) shows that the optical field intensity in the active layer is not significantly different for devices with and without a 10 nm PMMA interlayer.

To gain insight into why such a small surface area electrode is effective at extracting holes to the external circuit, steady-state and time-resolved photoluminescence (PL) measurements were made to probe the free charge carrier dynamics [17]. The structures probed comprised a very thin (4 nm) PCDTBT film supported on: (1) ITO/Au NP/PMMA/MoO_{3-x}, (2) ITO/PMMA/MoO_{3-x} and (3) ITO/MoO_{3-x} and the results are given in **Figure 5**. In all cases the PL emission peak is at a wavelength of ~710 nm (Figure 5 and Figure S8) which corresponds to the HOMO-LUMO gap in PCDTBT [18]. The PL decay time for this transition for PCDTBT

on ITO/AuNPs/PMMA/MoO_{3-x} is substantially less than that on ITO/MoO_{3-x} at 1.58 ns *vs* 2.40 ns, and less than half that for the control PCDTBT on ITO/ PMMA/MoO_{3-x}, which shows that AuNPs are able to efficiently extract charges from the PCDTBT layer even when sparsely distributed in the PMMA layer [19].

Previous work by our group has shown that geometric electric field enhancement at nanoscale protrusions on electrode surfaces can facilitate efficient charge carrier extraction in OPVs from a volume of the photoactive layer with a footprint many times that of the protrusion footprint[11b]. What is different here is that: (i) the metal protrusions are embedded in an insulating matrix, although geometric electric field enhancement can still occur because PMMA is an insulator; (ii) the conductive area in direct contact with the semiconductor is < 1% of that in the former; (iii) the AuNP density needed to achieve optimal performance is ~20 times lower (36 particles per μm^2 *vs* 720 protrusions per μm^2)[11b].

Electric field simulations performed using finite-element modelling (**Figure 6** and Figure S9) show that the static electric field is substantially enhanced where the AuNPs protrude from the PMMA surface due to geometric field enhancement, which would be expected to assist hole-extraction. However, the volume of the bulk-heterojunction layer which experiences this enhanced electric field is very small and so the increased electric field immediately above AuNPs cannot on its own explain why hole-extraction is so efficient in this context. Efficient localized extraction of holes at specific sites across the electrode surface would however establish a concentration gradient of holes laterally in the bulk-heterojunction layer, which would result in a diffusion current towards the site of the AuNPs. Indeed, in the complex interpenetrating network of the PCBTBT:$PC_{70}BM$ bulk-heterojunction the domain sizes are of the order of 4.2-4.6 nm [12], and so the concentration gradient established at the electrode interfaces must play some role in the efficient extraction of charge carriers by the electrodes [20] since the electric field falling across the photo-active layer at maximum power-point is low. It is therefore feasible that the same underlying process is operating to enable efficient hole-

extraction in this case, which is consistent with the fact that optimal device efficiency is achieved when the inter-particle separation is approximately twice that of the optimal BHJ thickness for devices.

2.3 High performance OPVs

Many high performance OPVs use selective charge transport layers with conductivity substantially higher than that of MoO_{3-x}, which enables their thickness to be increased so they can also serve as optical spacers [21]. The most widely used electron-selective layer is ZnO which is typically used with a thickness in the range 30-70 nm [22]. When deposited from a colloidal solution with low temperature annealing, as in this case, the conductivity of ZnO is at least an order of magnitude higher than evaporated MoO_{3-x}, although is still very resistive [23], as is evident from the current map in **Figure 7a** recorded using a c-AFM. Based on the findings for the aforementioned PCDTBT:$PC_{70}BM$ device study, and the higher conductance of the ZnO charge transport layer (resulting from the higher conductivity of ZnO and greater film thickness) OPV devices using an ITO/AuNP/PMMA/ZnO electrode with an average AuNP distance in the PMMA layer of 237 nm should perform as well as those without. To test this prediction devices with the ternary photoactive active layer; PCE12:ITIC-m:$PC_{70}BM$ were fabricated and tested. The optimized thickness for this high performance BHJ OPV is ~110 nm, which is very similar to that of PCBTBT:$PC_{70}BM$ based OPV devices. In this case the device architecture is; ITO/AuNPs (inter-particle distance 237 nm)/ PMMA (10nm)/MoO_{3-x}(5nm)/ZnO(30nm)/PCE12:ITIC-m:$PC_{70}BM$(100nm)/MoO_{3-x}(10 nm)/Ag(100 nm) and the AuNP/PMMA electrode is extracting electrons. The thin n-type MoO_{3-x} layer is kept in place to ensure that the PMMA is not dissolved during ZnO deposition and does not significantly adversely affect device performance. It is tentatively suggested that the inclusion of this high electron affinity interlayer [24], which is normally used to facilitate hole-extraction in OPVs, is tolerated because the ZnO layer is sufficiently n-type for the depletion region formed at the

MoO_3-ZnO interface to be narrow enough for electrons to efficiently tunnel from the ZnO conduction band into the MoO_3 conduction band. Indeed, we have previously shown that WO_3, which has a very similar electronic structure to MoO_3 (including a very large electron affinity), can severe an electron transport material in OPVs. [25]

Unlike OPVs based on PCDTBT:$PC_{70}BM$, devices based on a PCE12:ITIC-m:$PC_{70}BM$ light harvesting layer exhibit optimal performance upon first testing both with and without a AuNP/PMMA layer. However, in this case all electrodes are annealed at 120°C as part of the ZnO film deposition procedure, which is evidently sufficient to improve conductance at the site of the AuNPs in the PMMA film. As expected devices with a PMMA layer without AuNPs exhibit negligible photocurrent: Figure S11. As in the previous case, there is no significant difference in the shape of the EQE spectra for devices with and without the AuNP/PMMA interlayer (Figure 7c and Figure S12). Modelling of the optical intensity in devices with and without a 10 nm layer of PMMA (Figure S13) shows that the optical field intensity in the photoactive layer is actually fractionally higher for devices without a PMMA layer (reference device) in the region of 650-750 nm and so there is no advantage to the inclusion of the 10 nm PMMA layer in terms of the light distribution within the device.

Similar to the case of PCDTBT:$PC_{70}BM$ based OPVs, devices with AuNPs/PMMA electrodes perform at least as well as the reference devices. However, a statistical analysis of the device performance data [26] (without omitting any outliers from 18 individual devices) shows a narrower distribution of all the parameters in the devices with the small area Au/PMMA electrode: **Figure 8**. The much narrower spread in V_{oc} is common to devices based on ITO/AuNP/PMMA and is consistent with the effect of geometric electric field enhancement, which operates to suppress electron-injection by the ITO/AuNP/PMMA electrode in the dark for voltages less than the built-in voltage[11b].

The far-field transmission and reflectance spectra for the electrodes with and without AuNPs in the PMMA layer (Figure S14) show that the AuNPs give rise to substantial parasitic

absorption. Even though the AuNPs are sparsely distributed in the PMMA films they have a large absorption cross-section due to excitation of the localized surface plasmonic resonance in the wavelength range 500-600 nm. Consequently, it is reasonable to expect that if the AuNPs were replaced with conducting particles that did not result in substantial parasitic absorption, these low area electrodes would outperform the reference devices.

3. Conclusion

This study has shown that, contrary to conventional wisdom, efficient charge carrier extraction in OPVs based on bulk-heterojunction light harvesting layers does not require a large contact area between the semiconductor layers and the electrodes. We have shown that ~99% of the electrode surface can in fact be insulating without degrading the efficiency of charge carrier extraction to the external circuit, provided the spacing of the conducting areas is less than or equal to twice the optimal thickness of the BHJ layer. These finding open the door to the use of a large pallet of materials for optical spacers and charge transport layers based on a low density of conducting particles (such as graphene, carbon-nanotubes and metal nanoparticles) embedded in a wide band gap insulating matrix, the latter of which can be selected for its optical and mechanical properties without concern for its electrical properties. In the context of transparent electrodes based on optically thin metal films, reducing the contact area between the metal electrode and the organic photoactive layer will also reduce optical losses due to metal-induced quenching of excitons.

4. Experimental Section

All materials were purchased from Sigma-Aldrich unless otherwise stated. The materials and solvents were used as received without further purification. The solution of as received AuNPs was concentrated where necessary through centrifugation and removal of solvent. ITO/Glass

was purchased from Thin Film Devices, Inc (ITO thickness of 145 nm ± 10 nm, sheet resistance 15 ± 3 Ω sq−1) and glass substrates from Academy.

4.1 Monolayer formation and Au NP deposition

The substrates (silicon, glass or indium tin oxide (ITO) coated glass) were exposed to 95% (3-mercaptopropyl)trimethoxysilane (MPTMS) vapour for 2 hrs for a monolayer of MPTMS to form on the surface of the substrate. As received AuNP solution was concentrated by centrifuging at 8000 rpm for 30 min and subsequent removal of the solvent. The concentrated solutions were then drop cast onto ITO/Glass and left for variable times at 80°C to obtain different NP densities (Device 1: x2 concentrated solution annealed for 1 min, Device 2: x2 concentrated solution annealed for 3 min , Device 3: x2 concentrated solution annealed for 5 min , Device 4: x3 concentrated solution annealed for 1 min, Device 5: x3 concentrated solution annealed for 3 min , Device 6: x3 concentrated solution annealed for 5 min , Device 7: x4 concentrated solution annealed for 5 min). The films were then washed with de-ionised water to remove surfactants and other carbonaceous compounds present in the original AuNP solution post annealing at 100°C for a further 10 min. All steps were performed in air.

4.2 Device fabrication

Substrate Cleaning: Various substrates (Glass, ITO/Glass) were cleaned in an ultrasonic bath in diluted solutions of surfactant (Helmanex II), deionized water, acetone, and IPA for 10 min each followed by drying with a nitrogen gun and UV/O_3 treatment for 15 min (Novascan Technologies. Inc. PSD-UVT).

Preparation of active layers and fabrication of devices were carried out in a nitrogen filled glove box. Metals and metal oxides were thermally evaporated using a CreaPhys Organic Molecular evaporator located in the same glove box (< 3 x 10^{-6} mbar). The thickness of deposited films was monitored using a calibrated quartz - crystal microbalance mounted adjacent to the substrate.

4.2.1 Active layer preparation:

PCDTBT:$PC_{70}BM$ (1:4)

4.00 mg of PCDTBT was added to 1 ml of chlorobenzene and was left stirring overnight at 80°C. A weight of 16.00 mg of $PC_{70}BM$ was then added and stirred at 80°C for further 2 hrs. The solution was cooled to room temperature and filtered through a 0.2 µm PVDF micro filter prior to spin coating.

PCE12:ITIC-m: $PC_{70}BM$ (1:1:0.2)

10.00 mg of PCE12 (poly[(2,6-(4,8-bis(5-(2-ethylhexyl)thiophen-2-yl)-benzo[1,2-b:4,5-b']dithiophene))-alt-(5,5-(1',3'-di-2-thienyl-5',7'-bis(2-ethylhexyl)benzo[1',2'-c:4',5'-c']dithiophene-4,8-dione)]), 10.00 mg of ITIC-m (3,9-bis(2-methylene-((3-(1,1-dicyanomethylene)-6/7-methyl)-indanone))-5,5,11,11-tetrakis(4-hexylphenyl)-dithieno[2,3-d:2',3'-d']-s-indaceno[1,2-b:5,6-b']dithiophene), and 0.20 mg of $PC_{70}BM$ was added to 1.1 ml of chlorobenzene mixed with 11 µl of DIO (1,8-diiodooctane) and was left stirring for 4 hrs at 70°C. The solution was cooled to room temperature prior to spin coating.

Fabrication of device type 1: Freshly deposited AuNPs on ITO/Glass were exposed to UV/O_3 for 13 min. Then a solution of 3.5 mg ml^{-1} of PMMA in toluene was spun cast (drop then spin) at 3000 rpm for 60s onto the same substrate prior to exposure to UV/O_3 for a further 3 min. This deposition condition and post-deposition etching step yields a PMMA thickness of ~10 nm, as verified from cross-section analysis of scored films using an AFM, and exposes the top of the AuNPs (Figure 2). A 5nm thick film of MoO_{3-x} is then deposited at a rate of 0.1 Å s^{-1}. The active layer of PCDTBT:$PC_{70}BM$ was then spun at 700 rpm for 2 min and the films were annealed at 80°C for 10min. 3.5 nm of BCP (1 Å s^{-1}) and 70 nm Al (2 Å s^{-1}) was evaporated was evaporated through a shadow mask defining an electrode area of 0.06 cm^2. Reference devices were made using the same layer thicknesses.

Fabrication of device type 2: Freshly deposited AuNPs on ITO/Glass were exposed to UV/O_3 for 13 min. Then a solution of 3.5 mg ml-1 of PMMA in toluene was spun at 3000 rpm for 60s on AuNP deposited ITO/Glass prior to exposure to a UV/O_3 for a further 3 min. The thickness

of the formed PMMA layer is 10 nm. A 5nm thick film of MoO_{3-x} is then deposited at a rate of 0.1 Å s^{-1}. A 0.7% w/v ZnO solution in IPA (Infinity PV) was spun at 1000 rpm for 60 s followed by annealing at 120 °C for 10 min. The active layer of PCE12:ITIC-m: $PC_{70}BM$ was then spun at 2000 rpm for 1 min and the films were annealed at 110°C for 10min. 10 nm of MoO_{3-x} (0.1 Å s^{-1}) and 100 nm Ag (2 Å s^{-1}) was evaporated through a shadow mask defining an electrode area of 0.06 cm^2. Reference devices were made using the same layer thicknesses.

Characterization of OPV Devices: J-V characteristics of the devices were measured under a ABET technologies Sun 2000 Solar Simulator (1 sun, intensity 100 mW cm^{-2}, AM 1.5G) calibrated with a Newport 91150V silicon calibration cell (filter: KG5), using a Keithley 2400 source meter a custom Labview interface. Devices were measured through a pixel mask either with an area of 0.03 or 0.013 cm^2.

4.3 Transmission and reflectance measurements

Far-field transmission and reflectance measurements were carried out using either a 150 mm Spectralon Integrating Sphere coupled PerkinElmer LAMBDA high performance series of UV/vis spectrometer or a Cary 60 UV/Vis.

2.4 Tapping mode atomic force microscopy (AFM) and conducting AFM (c-AFM)

Imaging was performed using an Asylum Research MFP3D operated in AC (tapping) or contact mode. The samples were prepared on ITO/Glass functionalised with a monolayer of MPTMS prior to the deposition of AuNPs.

4.4 External Quantum Efficiency (EQE)

EQE measurements were carried out using a white light xenon arc lamp (Sciencetech SF150), monochromator (Photon Technology International), focusing and splitting lenses, current-voltage amplifier (Femto DHPCA - 100), lock - in amplifier (Stanford Research SR830 DSP), and a custom Labview interface.

4.5 Optical simulations

Electric filed distribution within devices was performed using the transfer matrix simulation software: Essential MacLeod V9.7 by Thin Film Center Inc. and finite element modelling: COMSOL.

4.6 Photoluminescence (PL) spectroscopy

Steady state and time resolved PL spectra were acquired using a Horiba Fluorolog®-3 instrument.

Supporting Information

Supporting Information is available from the Wiley Online Library or from the author.
All data supporting this study are provided as supplementary information accompanying this paper.

Acknowledgements

The authors wish to thank Dr. Michael Staniforth for the assistance with PL measurements and the Leverhulme Trust (Grant No. RPG-2015-044) for funding this project.

Received: ((will be filled in by the editorial staff))
Revised: ((will be filled in by the editorial staff))
Published online: ((will be filled in by the editorial staff))

References

[1] Y. Cui, H. Yao, J. Zhang, T. Zhang, Y. Wang, L. Hong, K. Xian, B. Xu, S. Zhang, J. Peng, Z. Wei, F. Gao, J. Hou, *Nat. Comm.* **2019,** 10, 2515.

[2] L. Meng, Y. Zhang, X. Wan, C. Li, X. Zhang, Y. Wang, X. Ke, Z. Xiao, L. Ding, R. Xia, H.-L. Yip, Y. Cao, Y. Chen, *Science.* **2018,** 361,1094.

[3] a) G. D. M. R. Dabera, M. R. R. Prabhath, K. T. Lai, K. D. G. I. Jayawardena, F. L. M. Sam, L. J. Rozanski, A. A. D. T. Adikaari, S. R. P. Silva, *Adv. Funct. Mater.* **2015**, 25, 4520; b) H.-J. Kim, K.-W. Seo, Y.-J. Noh, S.-I. Na, A. Sohn, D.-W. Kim, H.-K. Kim, *Sol. Energy Mater Sol. Cells.* **2015**, 141, 194; c) J. S. Kim, J. H. Park, J. H. Lee, J. Jo, D.-Y. Kim, K. Cho, *Appl. Phys. Lett.* **2007**, 91, 112111.

[4] a) S. Choi, W. J. P. Jr., B. Kippelen, *J. Appl. Phys.* **2009**, 106, 054507; b) R. Steim, F. R. Kogler, C. J. Brabec, *J. Mater. Chem.* **2010**, 20, 2499; c) K. Tvingstedt, O. Inganäs, *Adv. Mater.*

2007, 19, 2893; d) G. D. M. R. Dabera, K. D. G. I. Jayawardena, M. R. R. Prabhath, I. Yahya, Y. Y. Tan, N. A. Nismy, H. Shiozawa, M. Sauer, G. Ruiz-Soria, P. Ayala, V. Stolojan, A. A. D. T. Adikaari, P. D. Jarowski, T. Pichler, S. R. P. Silva, *ACS Nano.* **2013**, 7, 556; e) E. L. Ratcliff, B. Zacher, N. R. Armstrong, *J. Phys. Chem. Lett.* **2011**, 2, 1337; f) H. J. Pereira, O. S. Hutter, G. D. M. R. Dabera, L. A. Rochford, R. A. Hatton, *Sustainable Energy Fuels* **2017**, 1, 859.

[5] a) B. Cao, X. He, J. B. Sorge, A. Lalany, K. Ahadi, A. Afshar, B. C. Olsen, T. C. Hauger, M. H. Mobarok, P. Li, K. C. Cadien, M. J. Brett, E. J. Luber, J. M. Buriak, ACS Appl. Mater. Interfaces. 2017, 9, 38706; b) H. K. Yu, W. J. Dong, G. H. Jung, J.-L. Lee, ACS Nano. 2011, 5, 8026; c) Z. Lin, M. Zhu, J. Chang, C. Jiang, J. Zhang, J. Wu, W. K. Choi, C. Zhu, Energy Technol. 2015, 3, 906; d) J. Ham, J. Y. Park, W. J. Dong, G. H. Jung, H. K. Yu, J.-L. Lee, Appl. Phys. Lett. 2016, 108, 073903.

[6] C. Sachse, L. Müller-Meskamp, L. Bormann, Y. H. Kim, F. Lehnert, A. Philipp, B. Beyer, K. Leo, *Org. Electron.* **2013**, 14, 143.

[7] G. D. M. R. Dabera, M. Walker, A. M. Sanchez, H. J. Pereira, R. Beanland, R. A. Hatton, *Nat. Commun.* **2017**, 8, 1894.

[8] P. Schulz, J. O. Tiepelt, J. A. Christians, I. Levine, E. Edri, E. M. Sanehira, G. Hodes, D. Cahen, A. Kahn, *ACS Appl. Mater. Interfaces.* **2016**, 8, 31491.

[9] D. Cheyns, B. Kam, K. Vasseur, P. Heremans, B. P. Rand, *J. Appl. Phys.* **2013**, 4, 096104.

[10] a) L. Lu, Z. Luo, T. Xu, L. Yu, *Nano Lett.* **2013**, 13, 59; b) X. Yang, C.-C. Chueh, C.-Z. Li, H.-L. Yip, P. Yin, H. Chen, W.-C. Chen, A. K.-Y. Jen, *Adv. Energy Mater.* **2013**, 3, 666; c) K. K. Gandhi, A. Nejim, M. J. Beliatis, C. A. Mills, S. J. Henley, S. R. P. Silva, *J. Photon. Energy.* **2015,** 5, 057007.

[11] a) I. Vangelidis, A. Theodosi, M. J. Beliatis, K. K. Gandhi, A. Laskarakis, P. Patsalas, S. Logothetidis, S. R. P. Silva, E. Lidorikis, *ACS Photonics*. **2018**, 5, 1440; b) L.-J. Pegg, R. A. Hatton, *ACS Nano.* **2012**, 6, 4722.

[12] T. Wang, A. J. Pearson, A. D. F. Dunbar, P. A. Staniec, D. C. Watters, H. Yi, A. J. Ryan, R. A. L. Jones, A. Iraqi, D. G. Lidzey, *Adv. Funct. Mater.* **2012**, 22, 1399.

[13] a) D. C. Watters, J. Kingsley, H. Yi, T. Wang, A. Iraqi, D. Lidzey, *Org. Electron.* **2012**, 13, 1401; b) Y. Sun, C. J. Takacs, S. R. Cowan, J. H. Seo, X. Gong, A. Roy, A. J. Heeger, *Adv. Mater.* **2011**, 23, 2226.

[14] a) C. H. Peters, I. T. Sachs-Quintana, W. R. Mateker, T. Heumueller, J. Rivnay, R. Noriega, Z. M. Beiley, E. T. Hoke, A. Salleo, M. D. McGehee, *Adv. Mater.* **2012**, 24, 663; b)

A. Tournebize, A. Rivaton, J.-L. Gardette, C. Lombard, B. Pépin-Donat, S. Beaupré, M. Leclerc, *Adv. Energy Mater.* **2014**, 4, 1301530.

[15] B. J. Klein, *J. Phys. F Met. Phys.* **1973**, 3, 691.

[16] H. Yamauchi, S. Ito, K.-i. Yoshida, T. Itoh, Y. Tsuboi, N. Kitamura, H. Miyasaka, *J. Phys. Chem. C* **2013**, 117, 8388.

[17] J. R. Lakowicz, *Principles of Fluorescence Spectroscopy*, Springer, USA, **2007**.

[18] Z. Ahmad, S. M. Abdullah, D. Taguchi, K. Sulaiman, T. Manaka, M. Iwamoto, *Laser Phys.* **2014**, 24 105701.

[19] B. Gieseking, B. Jäck, E. Preis, S. Jung, M. Forster, U. Scherf, C. Deibel, V. Dyakonov, *Adv. Energy Mater.* **2012**, 2, 1477.

[20] V. M. Le Corre, A. R. Chatri, N. Y. Doumon, L. J. A. Koster, *Adv. Energy Mater.* **2017**, 7, 1701138.

[21] C. C. Chueh, M. Crump, A. K. Y. Jen, *Adv. Funct. Mater.* **2016,** 26, 321.

[22] H. J. Pereira, J. Reed, J. Lee, S. Varagnolo, G. D. M. R. Dabera, R. A. Hatton, *Adv. Funct. Mater.* **2018**, 28, 1802893.

[23] M. Caglar, S. Ilican, Y. Caglar, F. Yakuphanoglu, *Appl. Surf. Sci.* **2009**, 255, 4491.

[24] M. Kröger, S. Hamwi, J. Meyer, T. Riedl, W. Kowalsky, A. Kahn, *Appl. Phys. Lett.* **2009**, 95, 123301.

[25] O. Hutter and R. A. Hatton, *Adv. Mater.* **2015**, 27, 326-331.

[26] E. J. Luber, J. M. Buriak, *ACS Nano.* **2013**, 7, 4708.

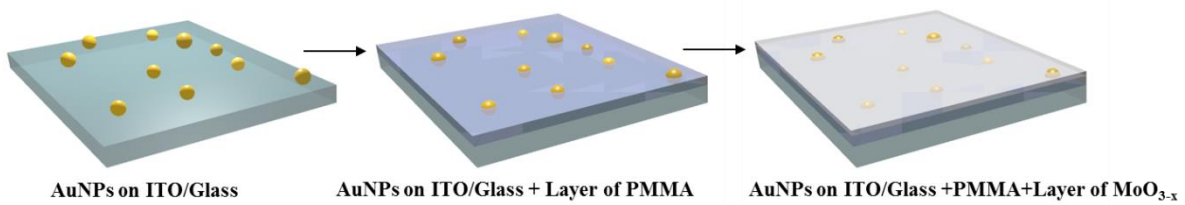

Figure 1. Schematic representation of the electrode fabrication process. The AuNPs tethered via MPTMS onto a substrate of ITO/Glass are partially covered with a 10 nm thick layer of PMMA followed by a 5 nm layer of MoO_{3-x} resulting in full/partial coverage of AuNPs.

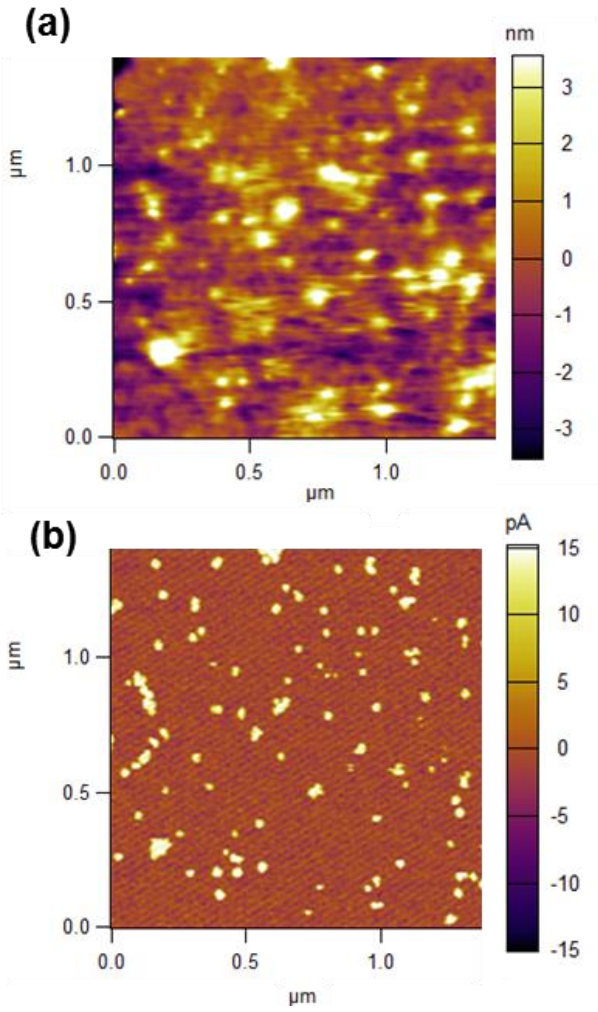

Figure 2. (a) Contact mode AFM topography image of a 1.3×1.3 µm area of an electrode comprising 10-20 nm diameter AuNPs embedded in a PMMA/MoO_{3-x} bilayer film supported on ITO glass from which the location of the AuNPs is just discernible as nanoscale bumps. (b) Corresponding conducting AFM image of (a) recorded with a tip bias of 10 mV, from which it is clear that the electrode surface is only electrically conductive at the site of AuNPs. Notably the images are of the surface of an electrode recovered from an actual OPV device after washing off the top opaque electrode and organic semiconductor layers.

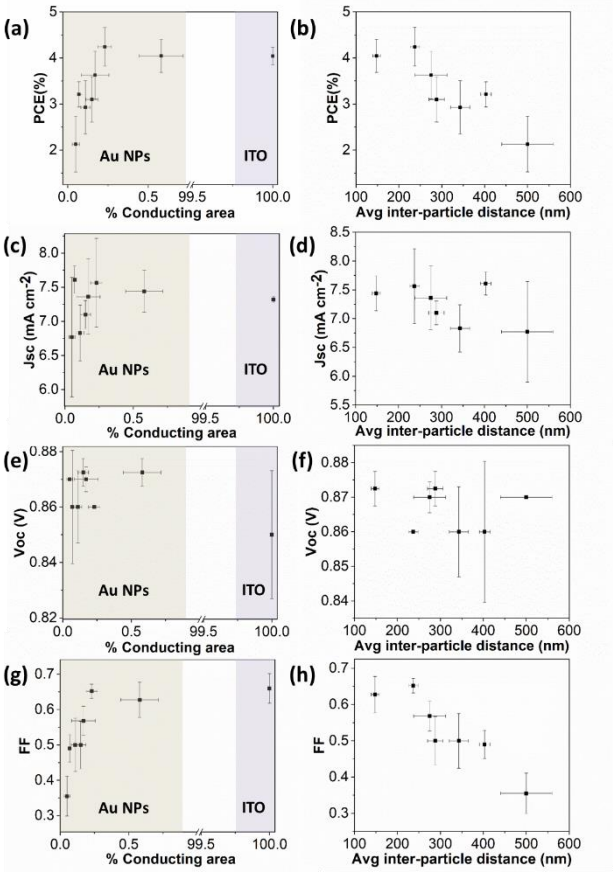

Figure 3. OPV device performance characteristics for devices with the architecture; ITO/AuNPs/PMMA/MoO_{3-x}/BCP/Al with varying Au NP concentrations. The percentage conducting area is calculated based on the AuNPs number density and the in-plane area of the average AuNP protruding from the PMMA film (Details of this calculation are provided in the Supporting Information). The area of the ITO electrode is assumed to be 100% for reference devices based on an ITO electrode. The device performance data presented are calculated based on 18 individual devices. Parts (a), (c), (e) and (g) show the device parameters *vs* percentage conducting area and (b), (d), (f) and (g) show the device parameters *vs* the average inter-particle separation (Details of this calculation are provided in the Supporting Information).

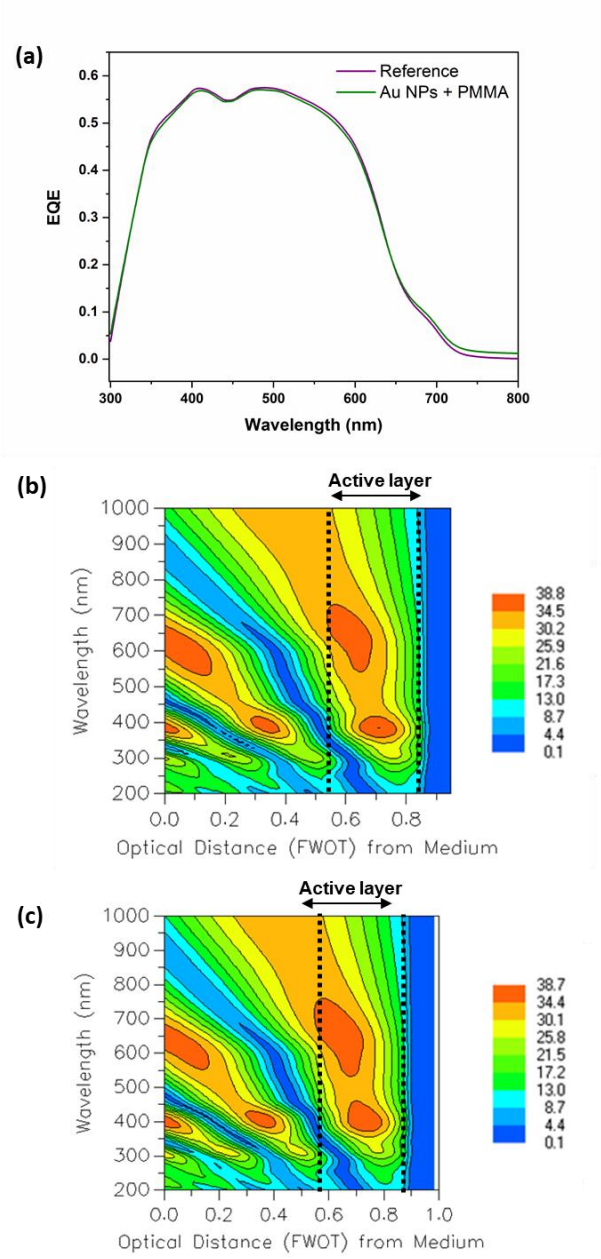

Figure 4. (a) EQE spectra corresponding to a reference device: ITO/MoO_{3-x}/PCDTBT:$PC_{70}BM$/BCP/Al and a test device ITO/AuNPs (inter-particle distance 237 nm)/ PMMA/MoO_{3-x}/PCDTBT:$PC_{70}BM$/BCP/Al. (b) and (c) are simulated contour plots of the optical field distribution inside a reference (no PMMA) and a test device (with PMMA) based on Macleod software.

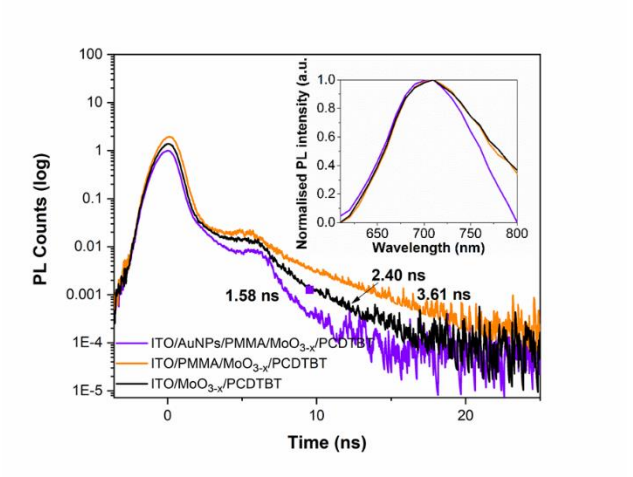

Figure 5. Steady state PL emission (inset) and time resolved decay spectra for a thin film of PCDTBT on electrodes: ITO/AuNPs/PMMA/MoO_{3-x}, ITO/ PMMA/MoO_{3-x} and ITO /MoO_{3-x}. The hump at ~6 ns is a minor secondary pulse from the excitation laser which is taken into account when fitting the decay characteristic.

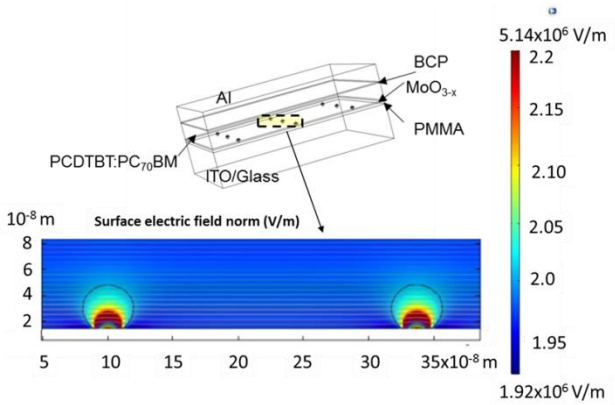

Figure 6. Finite-element modelling (COMSOL) of a device ITO/AuNPs (inter-particle distance 237 nm)/ PMMA(10 nm)/MoO_{3-x} (5 nm)/PCDTBT:$PC_{70}BM$(80 nm)/BCP(4.5 nm)/Al (100 nm) - inset. The E-field in the active layer is modelled across three parallel plane (*yz* direction) showing local E-field maxima in the vicinity of NPs, where the concentric circles converging on top of the particle represent the E-field lines and the parallel horizontal lines are equipotential lines.

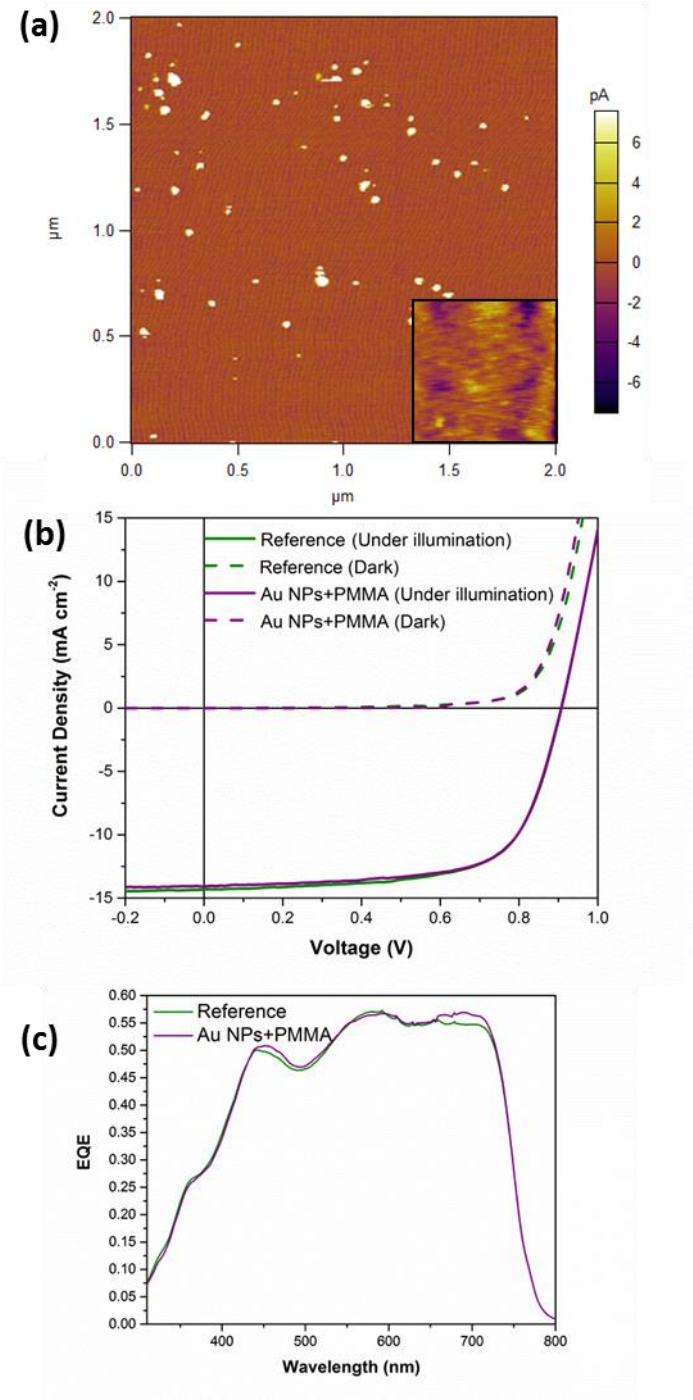

Figure 7. (a) c-AFM image of an electrode comprising 10-20 nm diameter AuNPs embedded in a PMMA/MoO_{3-x}/ZnO trilayer film supported on ITO glass. The area scanned is 2×2 µm and the tip bias is 300 mV. (inset) is the corresponding topography image of a) (b) *J-V* curves for the best performing reference (Electrode: ITO/MoO_{3-x}/ZnO) and test (Electrode: ITO/AuNPs/PMMA/MoO_{3-x}/ZnO) devices. (c) EQE spectra corresponding to the reference and test device in b).

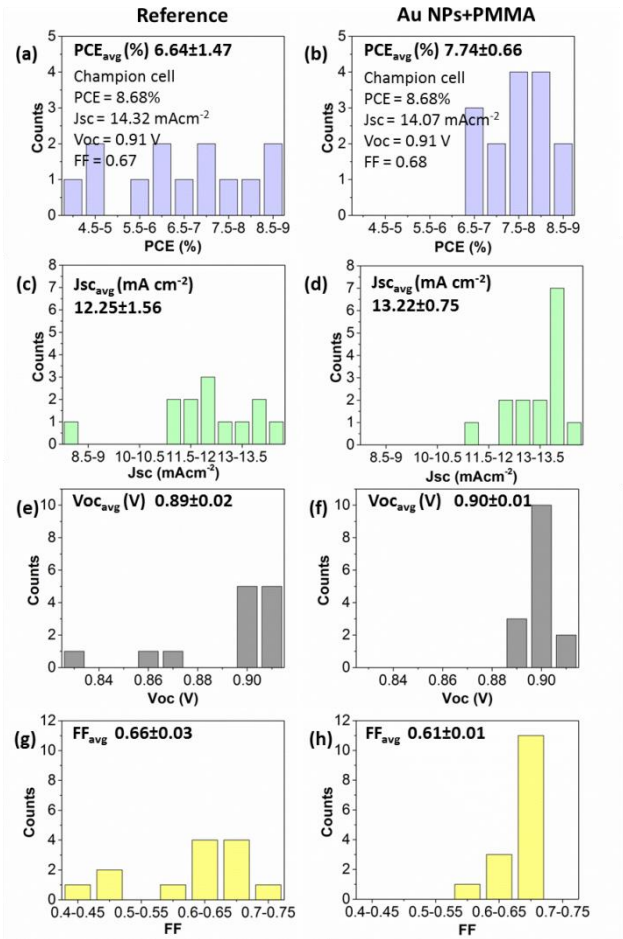

Figure 8. Distribution of device performance characteristics of reference and test devices with respective architectures: ITO/MoO_{3-x}/ZnO/PCE12:ITIC-m:$PC_{70}BM$/MoO_{3-x}/Ag and ITO/ AuNPs (inter-particle distance 237 nm)/PMMA/MoO_{3-x}/ZnO/PCE12:ITIC-m:$PC_{70}BM$/MoO_{3-x}/Ag. (a), (c), (e) and (g) are for reference devices and (b), (d), (f) and (g) are for test devices. The devices were measured as soon as the devices were illuminated with AM 1.5G irradiation as it gave the optimal performance.

Keywords: transparent electrode, nanoparticle electrode, organic photovoltaic, organic solar cell, gold nanoparticle, polymer solar cell

G. Dinesha M. R. Dabera, Jaemin Lee, Ross A. Hatton*

Title: An Electrode Design Rule for Organic Photovoltaics Elucidated Using a Low Surface Area Electrode

It is widely considered that charge carrier extraction in bulk-heterojunction (BHJ) organic photovoltaics is most efficient when the contact area between the semiconductor layers and electrodes is maximized. We show that ~99% of this area can be insulating without degrading the efficiency of charge carrier extraction, provided the spacing of the conducting areas is less than or equal to twice the optimal thickness of the BHJ layer.

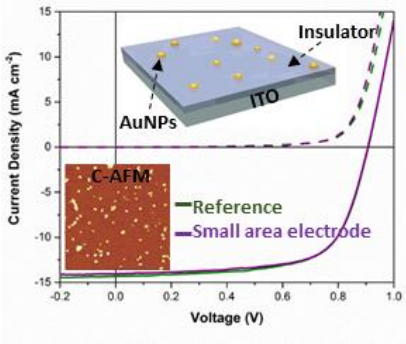

Supporting Information

An Electrode Design Rule for Organic Photovoltaics Elucidated Using a Low Surface Area Electrode

*G. Dinesha M. R. Dabera, Jaemin Lee, Ross A. Hatton**

Calculation of the average inter-particle distance (*x*)

The average inter-particle distance (*x*) was calculated from 3-4 separate AFM images for each NP loading, using the following method:

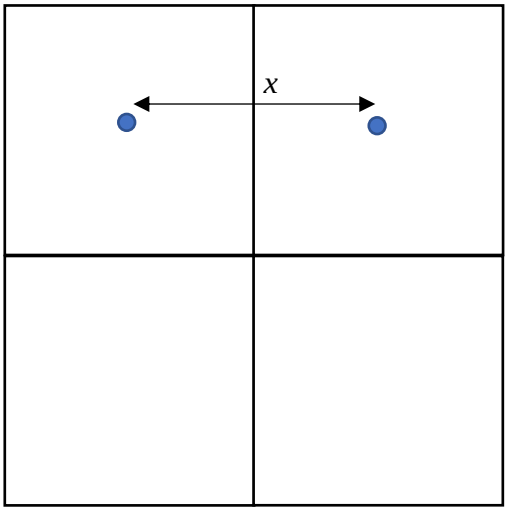

$$Area\ occupied\ by\ each\ NP\ (A) = \frac{Sample\ area}{Number\ \ of\ NPs\ in\ sample\ area}$$

The relation between A and the inter-particle distance, *x*, is:

$$A = x^2$$

Calculation of the percentage conducting area

In the current study the radius of the AFM tip (~20 nm) is greater than the diameter of the AuNPs (Figure S1), and so in the *x*-*y* image plane the AuNP size is greatly exaggerated and depends strongly on the geometry of the AFM tip. The height of the AuNPs measured across the centre of each AuNP does however give an accurate measure of the AuNP diameter. (See,

for example, Dabera *et al*. Nature Communications 8, 2017, 1894) Consequently, the following method was used to estimate the conducting area of the electrode:

The average diameter of AuNPs is 14 nm (Figure S1) and the AuNPs are embedded in a 10 nm thick PMMA layer, as illustrated below. The diameter of each AuNP (in the plane of the top surface of the PMMA layer) is 12.65 nm, which yields a geometric area of 126 nm^2 per AuNP.

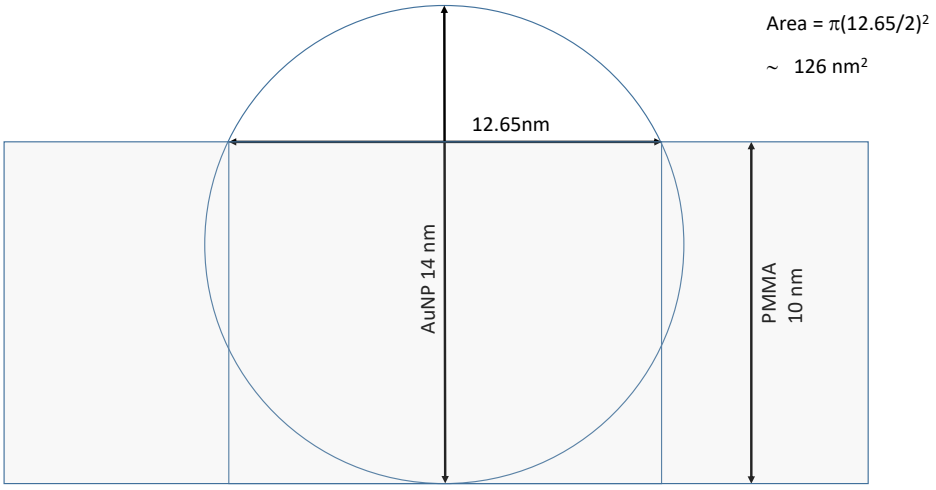

$$\text{Estimated percentage conducting area} = \frac{126\ \text{nm}^2 \times \text{Number of AuNPs in sample area}}{\text{Sample area}} \times 100\ \ \%$$

The error in this calculation is based on the variation in the AuNP density measured across nominally identical samples. For each AuNP loading 3-4 images were analysed and the error estimated based on the minimum and maximum values.

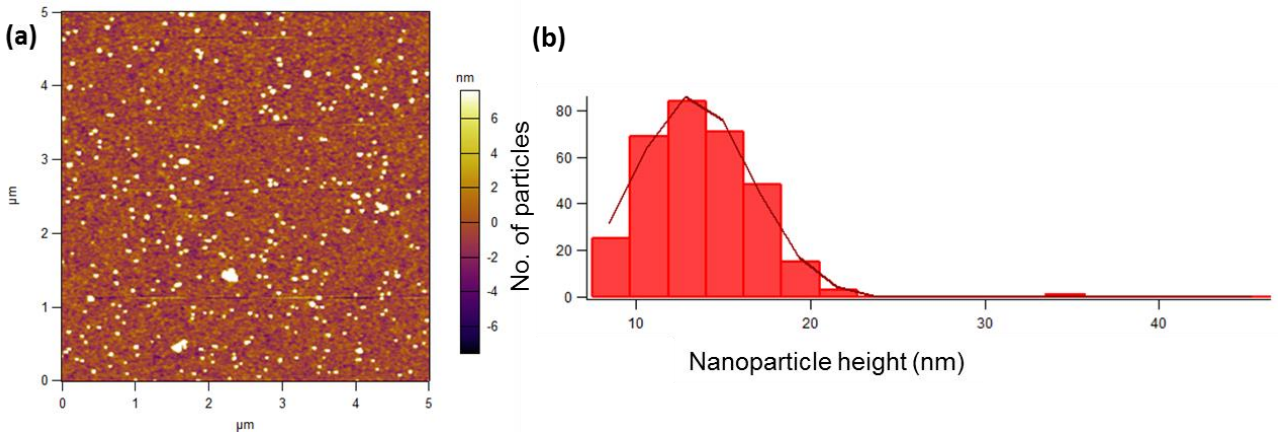

Figure S1. (a) Representative AFM image of AuNPs on a Si wafer. (b) Analysis of size distribution of AuNPs where the histogram is fitted with a Gaussian type curve. The mean diameter of particles ± 1 SD is 14 ± 4 nm.

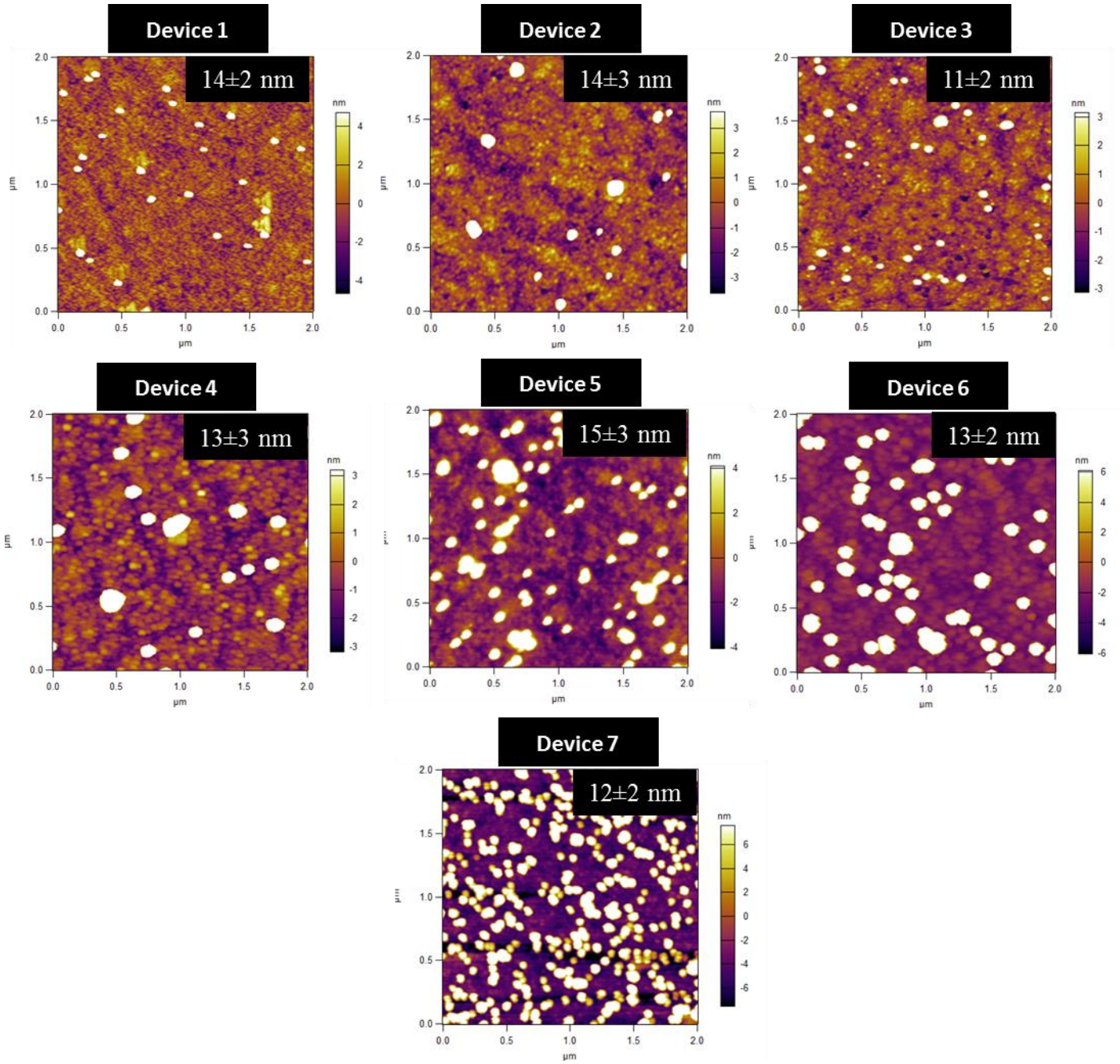

Figure S2. AFM images of the different AuNP concentrations used for OPV device fabrication. The AuNPs are tethered onto ITO glass with a monolayer of 3-mercaptopropyltrimethoxysilane. The mean AuNP diameter in each image is determined from the height of a cross-section through the centre of each particle, and is given in the top right corner of each image, from which it is evident that there is no significant difference in nanoparticle diameter between the images. The error in particle diameter is ± 1 standard deviation (SD).

Table S1. Device performance characteristics @ 50 min of illumination with varying concentrations of AuNPs. The device architecture is: ITO/MPTMS/AuNPs/PMMA/MoO_{3-x}/PCDTBT:$PC_{70}BM$/BCP/Al. The performance of reference device ITO/MoO_{3-x}/PCDTBT:$PC_{70}BM$/BCP/Al was recorded @0 min illumination. The error in the percentage conducting area and average inter-particle distance are derived from the difference between the maximum and minimum values in each data set.

Device		**% conducting area ±error**	**Average inter-particle distance (nm) ±error**		**Jsc (mA cm^{-2})**	**Voc (V)**	**FF**	**PCE (%)**
AuNPs+PMMA @ 50 min illumination	**1**	0.11±0.03	343±23	Avg	6.83±0.41	0.86±0.01	0.50±0.08	2.93±0.58
				Best	7.32	0.87	0.59	3.77
	2	0.05±0.02	500±60	Avg	6.77±0.87	0.87	0.36±0.05	2.13±0.60
				Best	8.04	0.87	0.46	3.20
	3	0.15±0.04	288±18	Avg	7.1±0.21	0.87±0.01	0.50±0.07	3.10±0.49
				Best	7.25	0.87	0.58	3.67
	4	0.07±0.01	403±13	Avg	7.61±0.19	0.86±0.02	0.49±0.04	3.21±0.27
				Best	7.72	0.87	0.53	3.53
	5	0.23±0.04	237±11	Avg	7.56±0.65	0.86	0.65±0.02	4.24±0.42
				Best	8.29	0.86	0.67	4.74
	6	0.17±0.09	274±37	Avg	7.36±0.55	0.87±0.02	0.57±0.04	3.63±0.52
				Best	7.92	0.87	0.63	4.36
	7	0.58±0.14	148±9	Avg	7.44±0.31	0.87±0.01	0.63±0.05	4.05±0.36
				Best	7.72	0.87	0.66	4.43
ITO @ 0 min illumination (no AuNPs)	**8**	100	NA	Avg	7.32±0.04	0.85±0.02	0.66±0.04	4.04±0.19
				Best	7.36	0.82	0.69	4.15

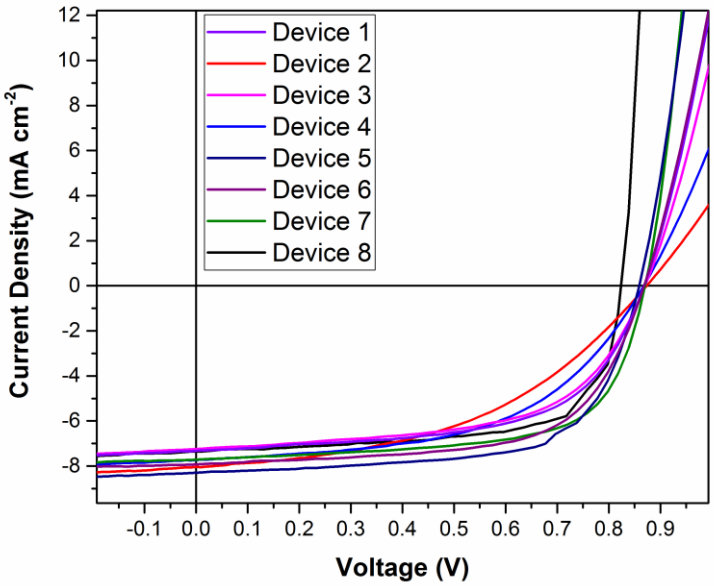

Figure S3. Device performance characteristics @ 50 min of illumination with varying concentrations of AuNPs. The device architecture is: ITO/MPTMS/AuNPs/PMMA/MoO_{3-x} /PCDTBT:$PC_{70}BM$/BCP/Al. The performance of reference device ITO/ MoO_{3-x} /PCDTBT:$PC_{70}BM$/BCP/Al was recorded @0 min illumination.

Table S2. Device performance characteristics within 50 mins of illumination of reference device 8 from Supplementary Table 1. The device architecture is: ITO/MoO_{3-x}/PCDTBT:$PC_{70}BM$/BCP/Al.

Duration of illumination	Jsc (mA cm^{-2})	Voc (V)	FF	PCE (%)
0 min	7.36	0.82	0.69	4.15
10 min	7.43	0.78	0.47	2.72
20 min	7.31	0.83	0.60	3.65
30 min	7.36	0.80	0.64	3.76
50 min	7.38	0.82	0.58	3.50

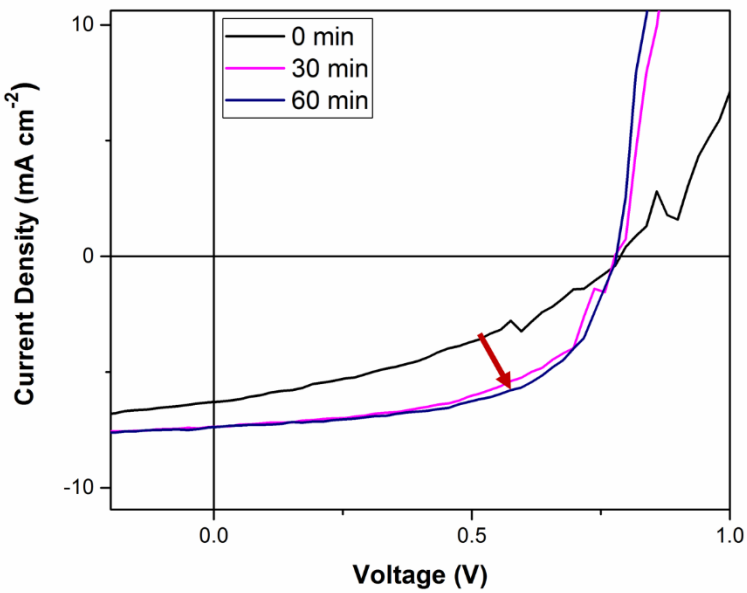

Figure S4. The evolution of *J-V* curves of a device of type: ITO/AuNPs/PMMA/MoO_{3-x} /PCDTBT:$PC_{70}BM$/BCP/Al under constant illumination. The curves demonstrate the improvement in *FF* and J_{sc} originating from a decrease in series resistance.

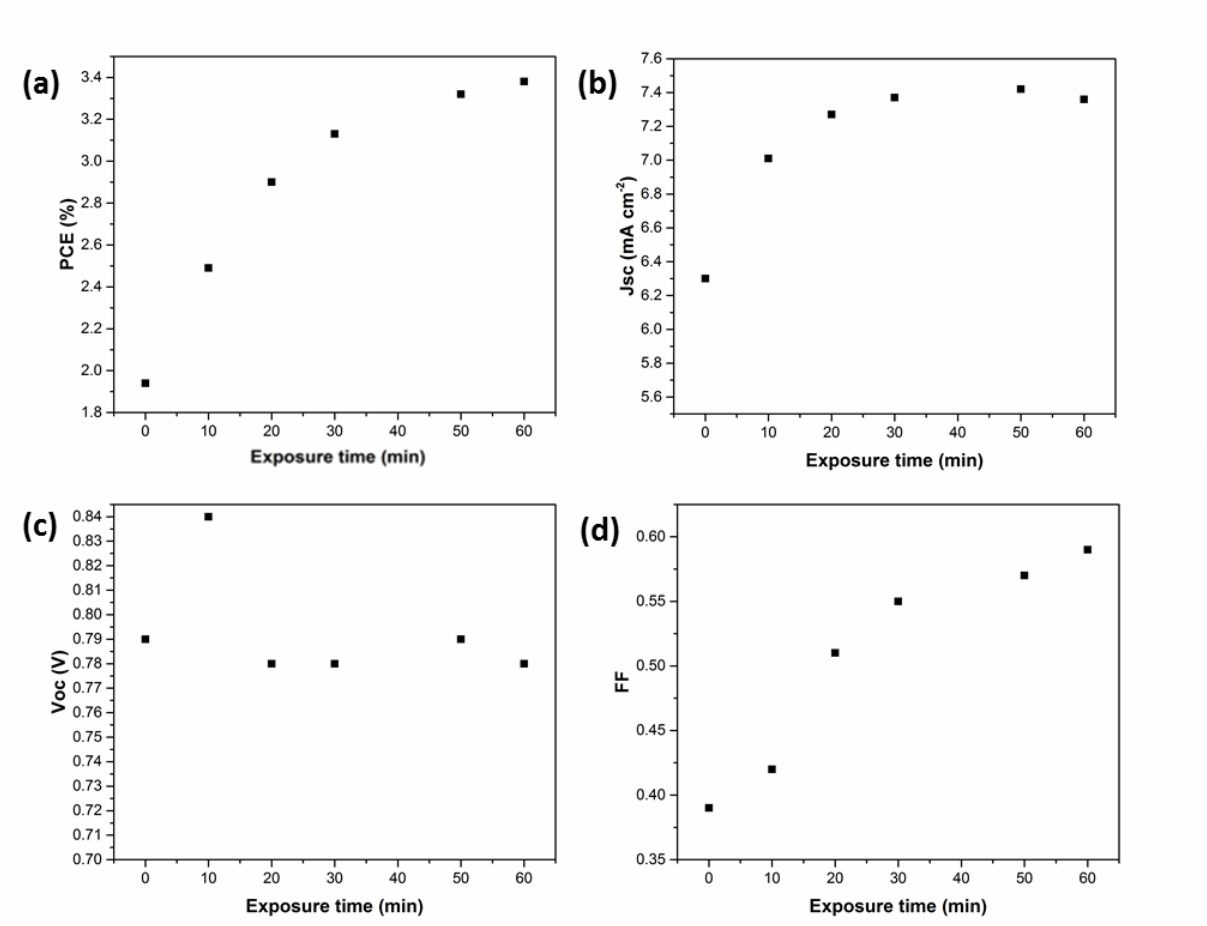

Figure S5. Device performance parameters of a typical ITO/AuNPs/PMMA/MoO_{3-x}/PCDTBT:$PC_{70}BM$/BCP/Al device under constant illumination.

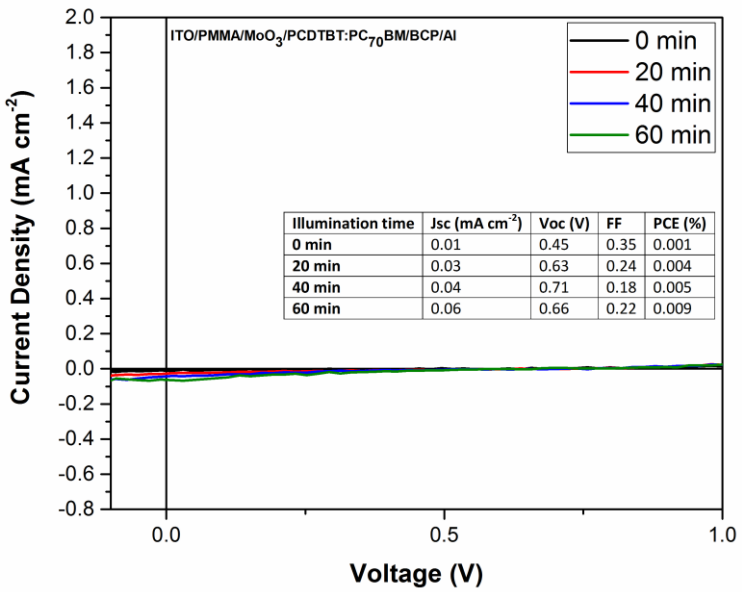

Illumination time	Jsc (mA cm^{-2})	Voc (V)	FF	PCE (%)
0 min	0.01	0.45	0.35	0.001
20 min	0.03	0.63	0.24	0.004
40 min	0.04	0.71	0.18	0.005
60 min	0.06	0.66	0.22	0.009

Figure S6. Device performance of ITO/PMMA/MoO_{3-x}/PCDTBT:$PC_{70}BM$/BCP/Al devices under constant 1 sun simulated solar illumination. The device performance data show that for devices with a PMMA layer without AuNPs there is a barrier to charge carrier extraction from the device consistent with the insulating nature of the 10 nm PMMA layer. The robustness of the PMMA layer towards continous illumination is also evident from the negligible J_{sc} even after 1 hr of illumination.

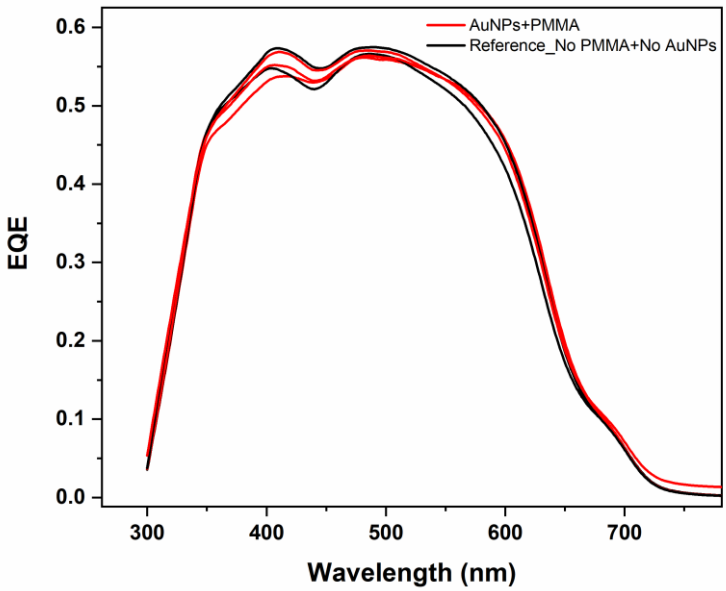

Figure S7. EQE spectra of OPV devices with ITO/AuNPs+PMMA/MoO_{3-x}/PCDTBT:$PC_{70}BM$/ /BCP/Al (red) and ITO/MoO_{3-x}/PCDTBT:$PC_{70}BM$/BCP/Al (black).

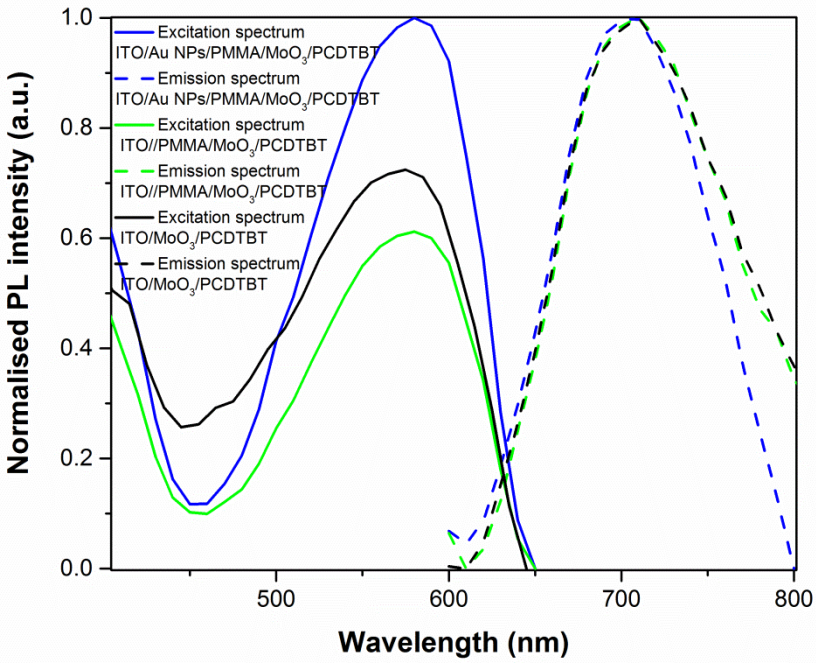

Figure S8. Static PL excitation (continuous lines) and emission (dotted lines) spectra of 3 types of electrodes used with a PCDTBT layer: (i) ITO/AuNPs+PMMA/MoO_{3-x}/PCDTBT, (ii) ITO/PMMA/MoO_{3-x}/PCDTBT and (iii) ITO/MoO_{3-x}/PCDTBT.

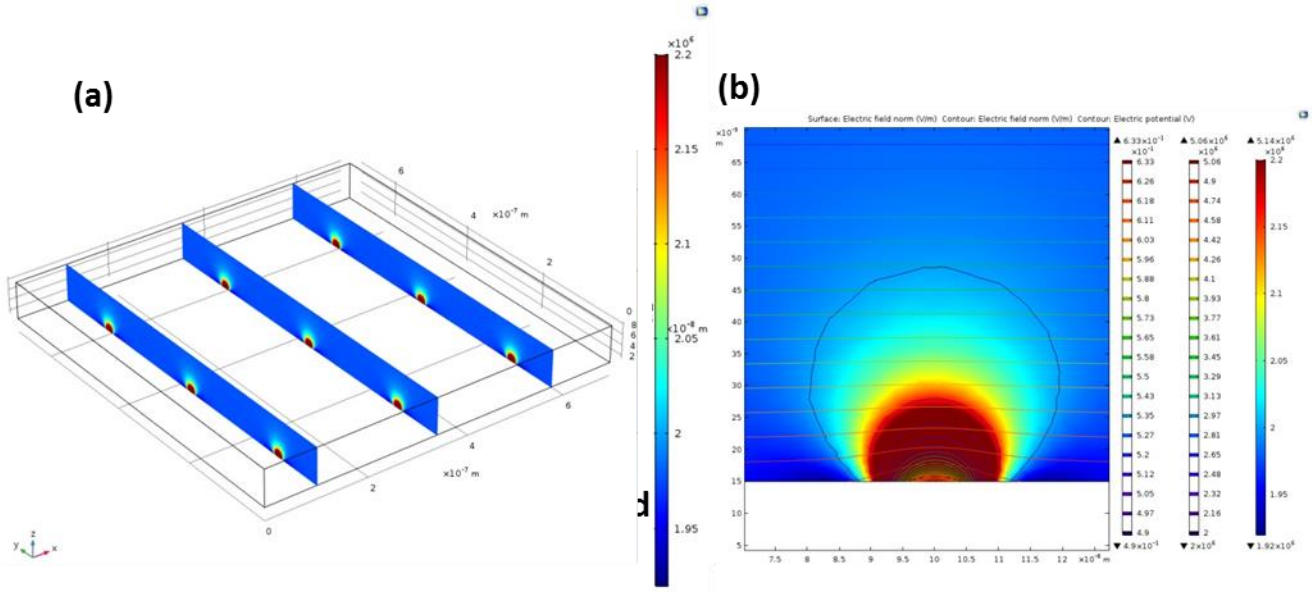

Figure S9. E-field simulation of a device: ITO/AuNPs+PMMA/MoO_{3-x} /PCDTBT:$PC_{70}BM$/BCP/Al using COMSOL. a) and b) show the interface between the AuNPs and active layer across different xyz planes.

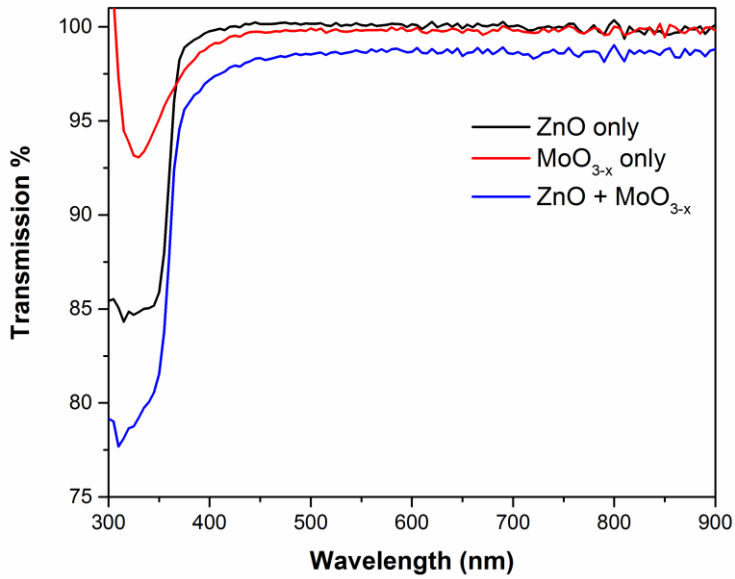

Figure S10. Total transmittance of films: 1) ZnO (30 nm), 2) MoO_{3-x} (5 nm) and 3) ZnO (30 nm) + MoO_{3-x} (5 nm). The films were deposited on glass.

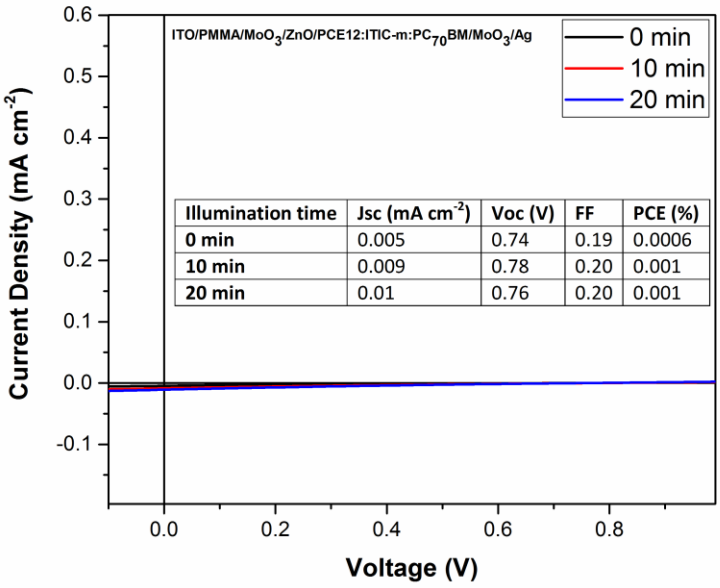

Illumination time	Jsc (mA cm^{-2})	Voc (V)	FF	PCE (%)
0 min	0.005	0.74	0.19	0.0006
10 min	0.009	0.78	0.20	0.001
20 min	0.01	0.76	0.20	0.001

Figure S11. Device performance of ITO/PMMA/MoO_{3-x}/ZnO/PCE12:ITIC-m:$PC_{70}BM$/ MoO_{3-x} /Ag devices under constant illumination.

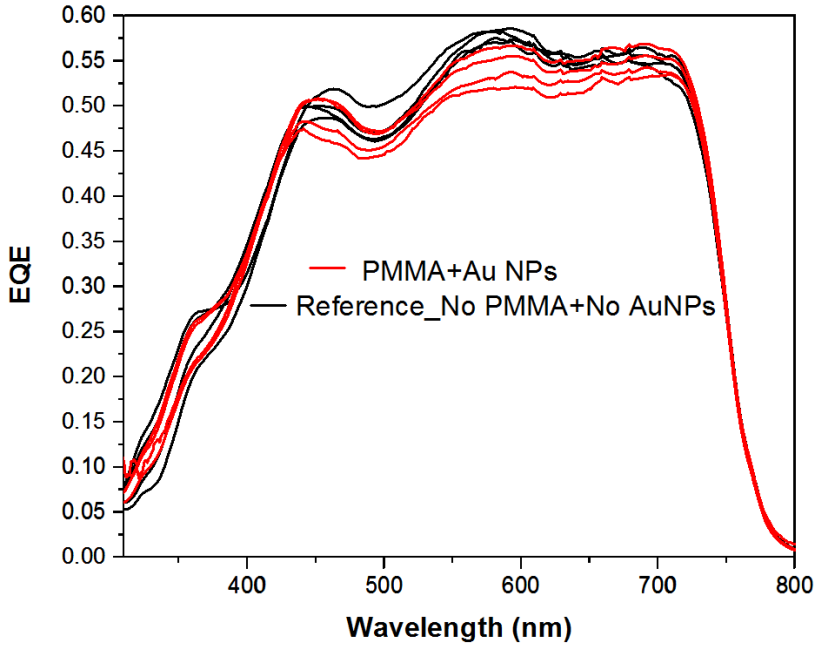

Figure S12. EQE spectra of devices with ITO/AuNPs+PMMA/MoO_{3-x}/ZnO/PCE12:ITIC-m:$PC_{70}BM$/MoO_{3-x} /Ag (red) and ITO/MoO_{3-x}/ZnO/PCE12:ITIC-m:$PC_{70}BM$/MoO_{3-x}/Ag (black).

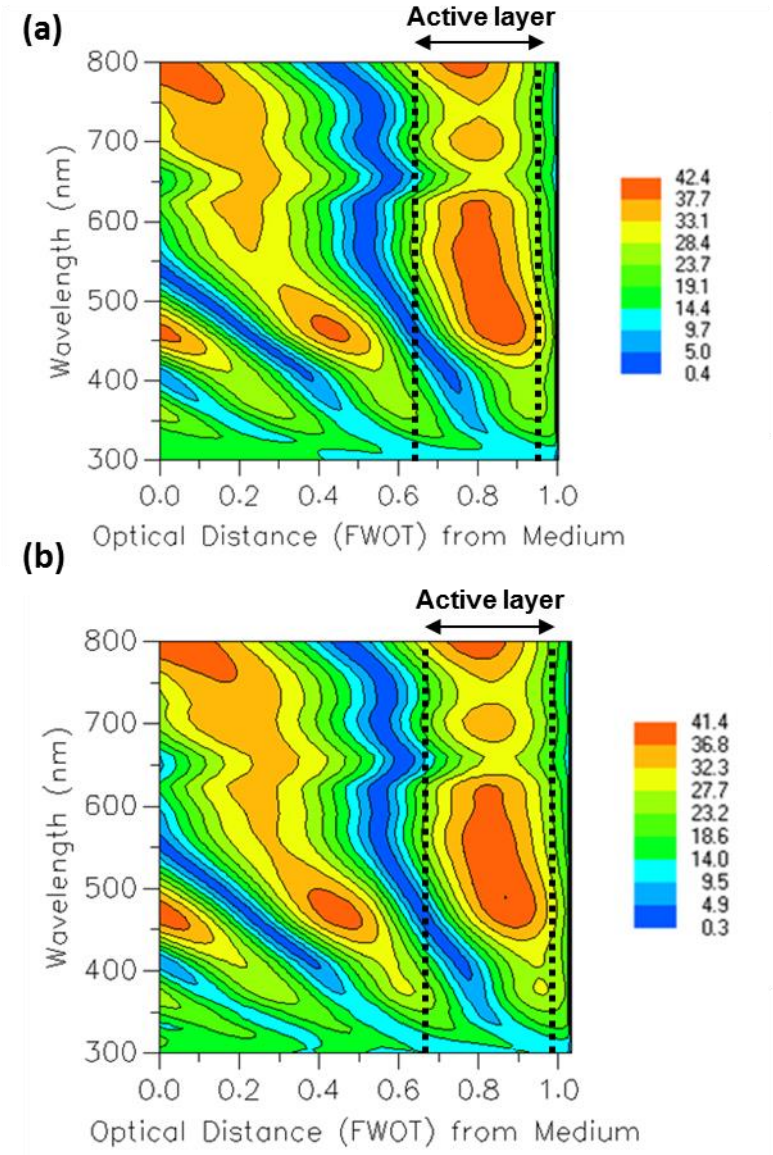

Figure S13. (a) and (b) are simulated contour plots of the optical field distribution inside a reference (ITO/MoO_{3-x}/ZnO/PCE12:ITIC-m:$PC_{70}BM$/MoO_{3-x}/Ag) and a test device (ITO/PMMA/MoO_{3-x}/ZnO/PCE12:ITIC-m:$PC_{70}BM$/MoO_{3-x}/Ag) based on Macleod software (N.B. presence of AuNPs cannot be simulated within the strength of the software).

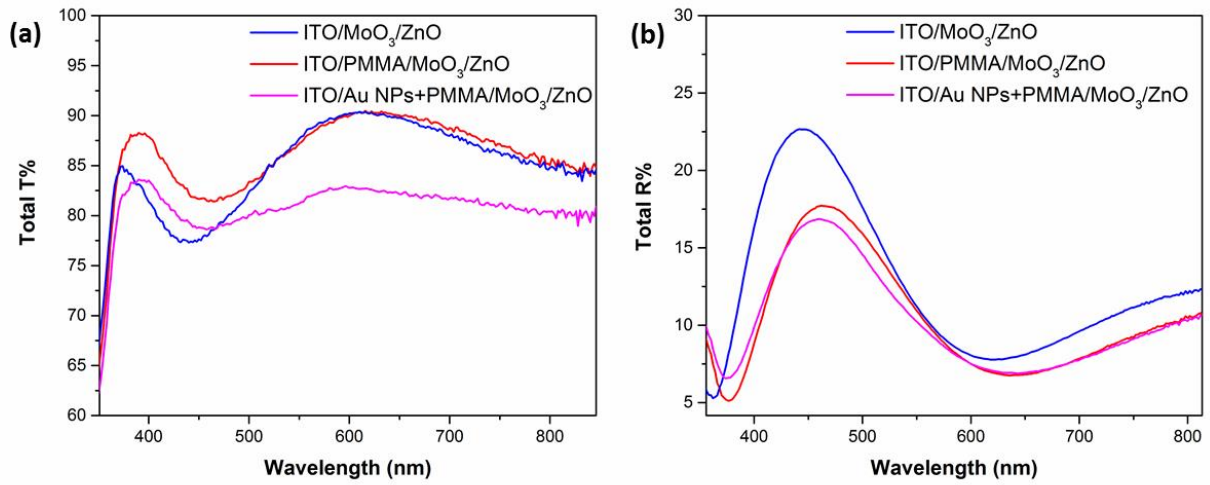

Figure S14. (a) UV/Vis transmission (T%) and (b) Reflectance (R%) spectra of films: ITO/MoO_{3-x}/ZnO, ITO/PMMA/MoO_{3-x}/ZnO and ITO/AuNPs/PMMA/MoO_{3-x}/ZnO to mimic light entering to the active layer through different electrode systems.

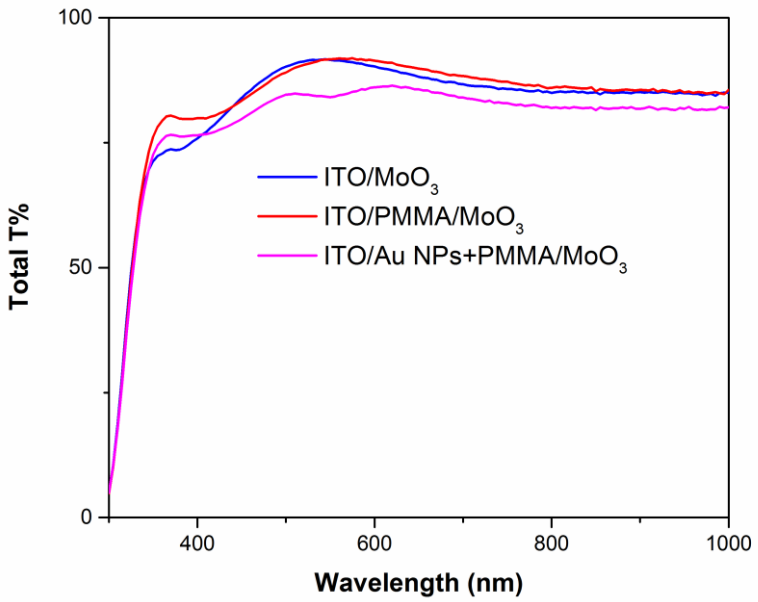

Figure S15. Total transmittance of electrodes: ITO/MoO_3-x (blue), ITO/PMMA/MoO_{3-x} (red) and ITO/AuNPs+PMMA/ MoO_{3-x} (pink).

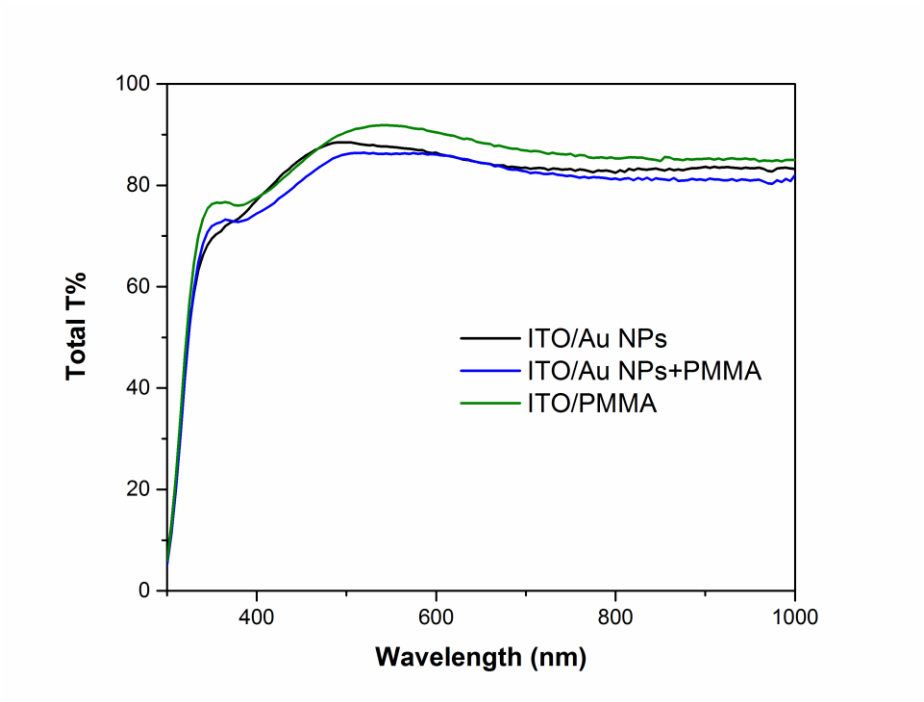

Figure S16. Total transmittance of electrodes: ITO/AuNPs (black), ITO/AuNPs+PMMA (blue) and ITO/PMMA (green).